Supporting Information

High-Entropy Alloy Nanocrystal Assembled by Nanosheets with d-d Electron Interaction for Superior Hydrogen Evolution Reaction

Min Wei[a], Yuyan Sun[a], Junyu Zhang[a], Fei Ai[a], Shibo Xi*[b], Jike Wang*[a]

* Corresponding authors

[a] The Institute for Advanced Studies, Wuhan University, Wuhan, 430072, China.

Email: Jike.Wang@whu.edu.cn

[b] Institute of Chemical and Engineering sciences, A*STAR (Agency for Science, Technology and Research) Singapore 627833, Singapore.

Email: xi_shibo@partner.nus.edu.sg

1. Materials

Nickel acetylacetonate (Ni(acac)$_2$), Platinum acetylacetone (Pt(acac)$_2$), Palladium acetylacetonate (Pd(acac)$_2$), Rhodium acetylacetonate (Rh(acac)$_3$), Molybdenum hexacarbonyl (Mo(CO)$_6$), Triethylene glycol (TEG), D(+)-Glucose, Triethylbenzylammonium (TEBA) are purchased by Aladdin.

1.1. Preparation of PtMoPdRhNi nanocrystals (PtMoPdRhNi NCs)

PtMoPdRhNi NCs were prepared by traditional one-step wet chemistry method. 0.025/0.075/0.125/0.175 mmol Ni(acac)$_2$, 0.025 mmol Pt(acac)$_2$, 0.025 mmol Pd(acac)$_2$, 0.025 mmol Rh(acac)$_3$, 0.125 mmol Mo(CO)$_6$, 600 mg TEBA were dissolved in 10 mL TEG under stirring for 4 hours. Then the mixed reacted in reaction still at 230 °C for 1 h, and then cooled down until room temperature. After that, the productions were washed with anhydrous ethanol several times, dried in vacuum for further used.

1.2. Preparation of PtMoPdRhNi nanoparticles (PtMoPdRhNi NPs)

PtMoPdRhNi NCs were prepared by traditional one-step wet chemistry method. 0.025 mmol Ni(acac)$_2$, 0.025 mmol Pt(acac)$_2$, 0.025 mmol Pd(acac)$_2$, 0.025 mmol Rh(acac)$_3$ and 0.025 mmol Mo(acac)$_2$ were dissolved in 10 mL TEG under stirring for 4 hours. Then the mixed reacted in reaction still at 230 °C for 1 h, and then cooled down until room temperature. After that, the productions were washed with anhydrous ethanol several times, dried in vacuum for further used.

2. Materials characterization

Transmission electron microscopy (TEM) images and elemental distribution spectrometer (EDS) mapping were captured using a JEM-ARM200F (JEOL, JAPAN) at 200 kV. The crystal structure and lattice parameters of PtMoPdRhNi NCs and Commercial Pt/C were characterized by X-ray powder diffraction (XRD, Rigaku Smartlab SE, Japan) which

was operated with Cu Ka radiation (k = 1.5405 Å) at 40 kV and 30 mA. The chemical state of PtMoPdRhNi NCs and commercial Pt/C were acquired through X-ray photoelectron spectroscopy (XPS ESCALAB 250XI) with an ESCALAB 250 Xi (Thermo Fisher Scientific, USA) using a monochromatic Al X-ray source. The content of Pt, Ni, Mo, Pd, Rh in catalyst is analyzed via the inductively coupled plasma-atomic emission spectroscopy (ICP-AES, Thermo Fisher Scientific, USA).

3. XAFS experiment and data processing

XAFS measurements at Pt L_3-edge and Ni K-edge in transmission mode was performed at the Singapore synchrotron light source (SSLS).

The raw data analysis was conducted using IFEFFIT software package according to the standard data analysis procedures. The spectra were calibrated, averaged, pre-edge background subtracted, and post-edge normalized using Athena program in IFEFFIT software package. The Fourier transformation of the k^3-weighted EXAFS oscillations, $k^3 \cdot \chi(k)$, from k space to R space was performed over a range of 3.5-11.5 Å^{-1} to obtain a radial distribution function. And data fitting was done by Artemis program in IFEFFIT[1].

4. Electrochemical test

The electrochemical activity of PtMoPdRhNi NCs for HER was measured in a three-electrode electrolytic cell using biopotentiostat (Pine, USA) equipped with a rotational disk electrode (RDE) system, in which a glassy carbon electrode covered with a thin film of catalyst was used as the working electrode, a reversible hydrogen electrode (RHE) and a graphite rod electrode were employed as the reference electrode and counter electrode, respectively. To evaluate the HER performance, PtMoPdRhNi NCs catalysts were mixed with Vulcan XC-72 carbon black (mass ratio is 1:1). 3.0 mg of the catalyst was dispersed in 2 ml of solution (1.5 ml of water, 0.48 ml of ethyl alcohol and 0.02 ml of 5 wt% Nafion). The electrodes had a

metal (HEAs or Pt) loading of 21.44 mg cm^{-2}. The hydrogen linear sweep voltammetry (LSV) was recorded in N$_2$-saturated 1.0 M KOH solution at a scan rate of 10 mV s^{-1}. The electrochemically active surface area (ECSA) of catalysts were reflected by electrochemical double-layer capacitance, C$_{dl}$, which was calculated from CV curves recorded in a potential range without Faradaic current at different scan rates from 20 to 100 mV s^{-1}. The anodic charging currents measured at desired potential vs. RHE was plotted as a function of the scan rate and from the slope, C$_{dl}$ was obtained. The accelerated durability tests (ADTs) were conducted in 1.0 M KOH solution through performing cyclic potential sweeps between 0 and -0.5 V vs. RHE at a scan rate of 100 mV s^{-1} for 50,000 cycles.

The H$_2$ product was measured by H-type electrolytic cell with three-electrode system. In order to accurately determine the actual amount of hydrogen generation, a systematic experiment was conducted by a closed HER device. Before experiment, the electrolyte was bubbled with Ar for at least 30 min. Then, the experiment was carried out. The product was taken every 11 min the and H$_2$ yield was measured precisely gas chromatography (GC) instrument. The Faradaic efficiency of catalysts is defined as the ratio of the amount of experimentally determined H$_2$ to that of the theoretically expected H$_2$ from the reaction. As for the theoretical value, it was assumed that 100% current efficiency occurs during the reaction, which means only the HER process was occurring at the working electrode. The theoretical amount of H$_2$ evolved was then calculated by applying the Faraday law, which states that the passage of 96485.4 C charge causes 1 equivalent of reaction[2,3].

In-situ surface-enhanced Raman spectroscopy (SERS) was performance with Renishaw (Confocal Raman Microscopy). The excitation wavelength was 633 nm from a He-Ne laser for 400-1500 cm^{-1} detection and 532 nm from a He-Ne laser for 1600-2100 cm^{-1} detection, and a 50× microscope for all Raman measurements.

5. DFT calculation details

Density-functional theory (DFT) containing spin polarization was implemented in the Vienna *ab-initio* simulation package (VASP)[4, 5]. The core-electron interactions were described by the projector-augmented wave (PAW) method[6]. And the exchange-correlation interaction was represented by Generalized gradient approximation with Perdew, Bruke and Ernzerhof (PAW-PBE)[7]. The plane wave function with a cutoff energy of 600 eV and 500 eV was used for bulk geometry and slab optimizations, respectively. The method of special quasirandom structure (SQS) was utilized for approximating the PtMoPdRhNi HEA, as SQS represent the best periodic approximation to the true disordered state[8]. It was generated from $Pt_{30}Mo_5Pd_{25}Rh_{25}Ni_{15}$ (1 1 1) surface by using Alloy Theoretic Automated Toolkit (ATAT)[9] code optimized by VASP. Fcc structure of metallic Pt (PDF#89-7382) was used as bulk model. A vacuum thickness of 15 Å was added to perpendicular the surface to avoid the image force between the periodic slab. The convergence criterion of energy and force were set to 1×10^{-5} eV and -0.02 eV·Å^{-1} in all calculation process, respectively. A k-points sampling 2x2x1 and 1x2x1 based on Gamma-centred Monkhorst-Pack were conducted for Pt (1 1 1) and PtMoPdRhNi bulk geometry calculation and slab structure relaxations. A four-layer slab model with supercell was built by cleave the (1 1 1) facet of metallic Pt and $Pt_{30}Mo_5Pd_{25}Rh_{25}Ni_{15}$, and the total number of atoms in Pt and $Pt_{30}Mo_5Pd_{25}Rh_{25}Ni_{15}$ are 120 and 160, respectively.

The adsorption energy was calculated according to formula $\Delta E_{ads}(H^*) = E_{slab+H}(H^*) - E_{slab} - 1/2E(H_2)$ and $\Delta E_{ads}(H_2O) = E_{slab+H2O}(H_2O) - E_{slab} - 1/2E(H_2O)$, where $E_{slab+O}(H^*)$, E_{slab}, $E(H_2)$, $E_{slab+H2O}(H_2O)$ and $E(H_2O)$ were represented the total energy of H adsorption on slab, the total energy of pure slab, the total energy of the hydrogen molecules in gas phase, the total energy of H_2O adsorption on slab and the total energy of H_2O molecules, respectively. And the Gibbs

free energy of intermediate at 300 K and 1atm was calculated by $\Delta G = \Delta E + \Delta ZPE - T\Delta S$, where ΔE_{abs}, ΔZPE, ΔS is adsorption energy, zero-point energy change and entropy change of adsorption of intermediates, respectively.

Based on Sabatier volcano, the equation

$$A = \sum_{i=1}^{Z} \left(\prod_{k=1}^{metals} f_k^{n_{ik}} \right) * exp\left(-\frac{|\Delta G_i - \Delta G_{opt}|}{k_B T} \right)$$

is applied to calculate the activity (A) of H* adsorption/desorption with different configuration in $Pt_{30}Mo_5Pd_{25}Rh_{25}Ni_{15}$, in which Z is the total number of surface configurations, f_k is the atomic fraction of element k, n_{ik} is the number of element k in the surface configuration i, ΔG_i is the modeled adsorption free energy for the ith surface configuration, ΔG_{opt} is the optimum adsorption free energy according to the Sabatier principle, k_B is Boltzmann's constant, and T is the absolute temperature[10]. The M-H bond length appears to be a good measure of M-H bond strength, and thus a great measure for ΔG_H[11]. Therefore, the contribution of constitute metals to the activity was estimated approximately, in which on-top adsorption configuration assumed the contribution of the nearest neighbor atom accounted for 100%, and hexagonal close packed configuration was weighted according to the reciprocal distance.
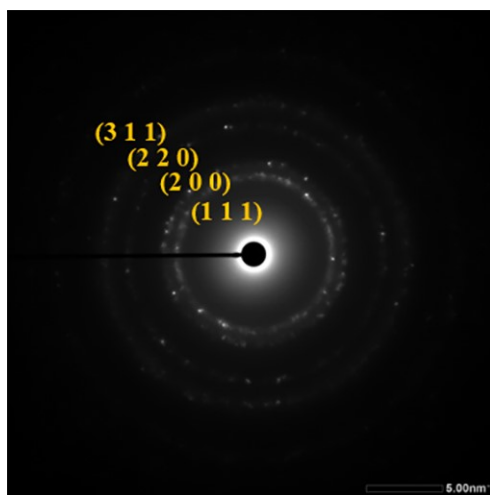
Figure S1. Selected area electron diffraction (SAED) image of $Pt_{28}Mo_6Pd_{28}Rh_{27}Ni_{15}$ NCs.

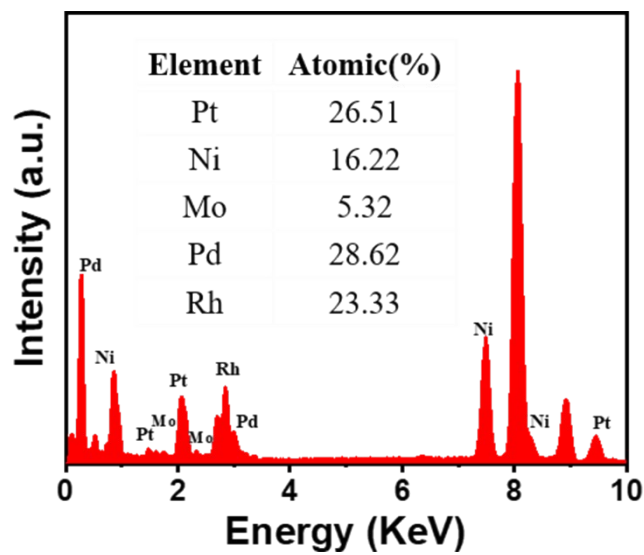**Figure S2.** EDS spectrum and the corresponding atomic ratio of $Pt_{28}Mo_6Pd_{28}Rh_{27}Ni_{15}$ NCs.

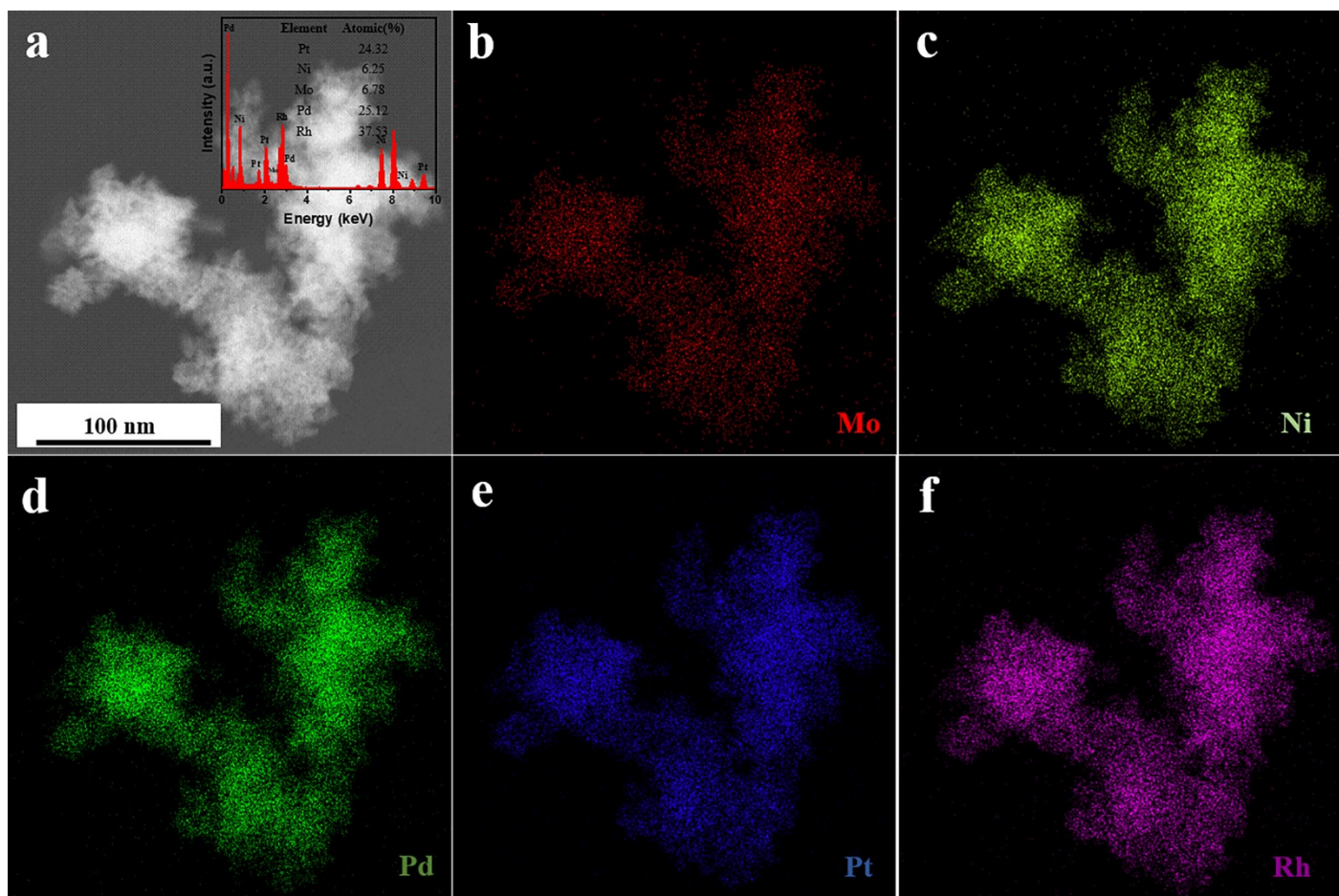**Figure S3.** (a) EDS spectrum and the corresponding atomic ratio, (b-f) elemental mapping of $Pt_{23}Mo_6Pd_{23}Rh_{43}Ni_5$ NCs.

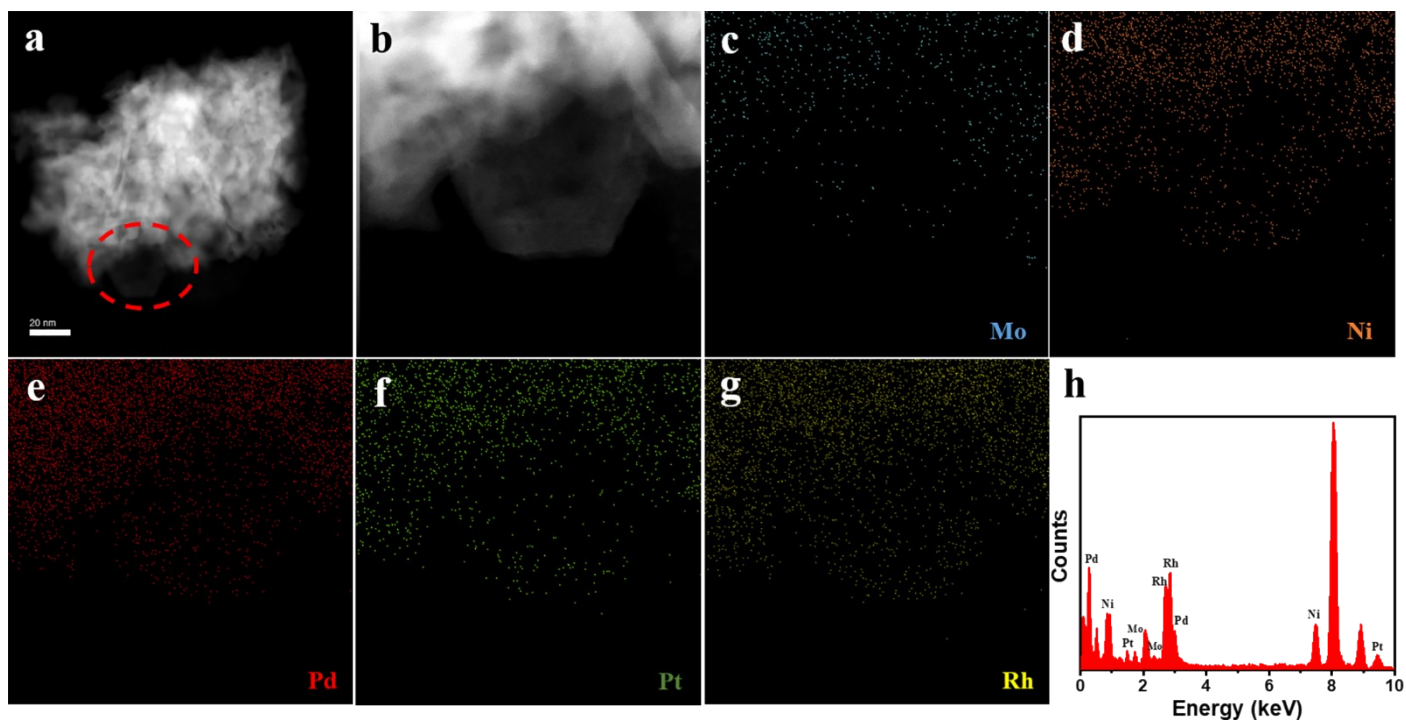**Figure S4.** (a) (b) HADDF images, (c-g) elemental mapping, and (h) EDS spectrum and the corresponding atomic ratio of $Pt_{33}Mo_6Pd_{33}Rh_{18}Ni_{10}$ NCs.
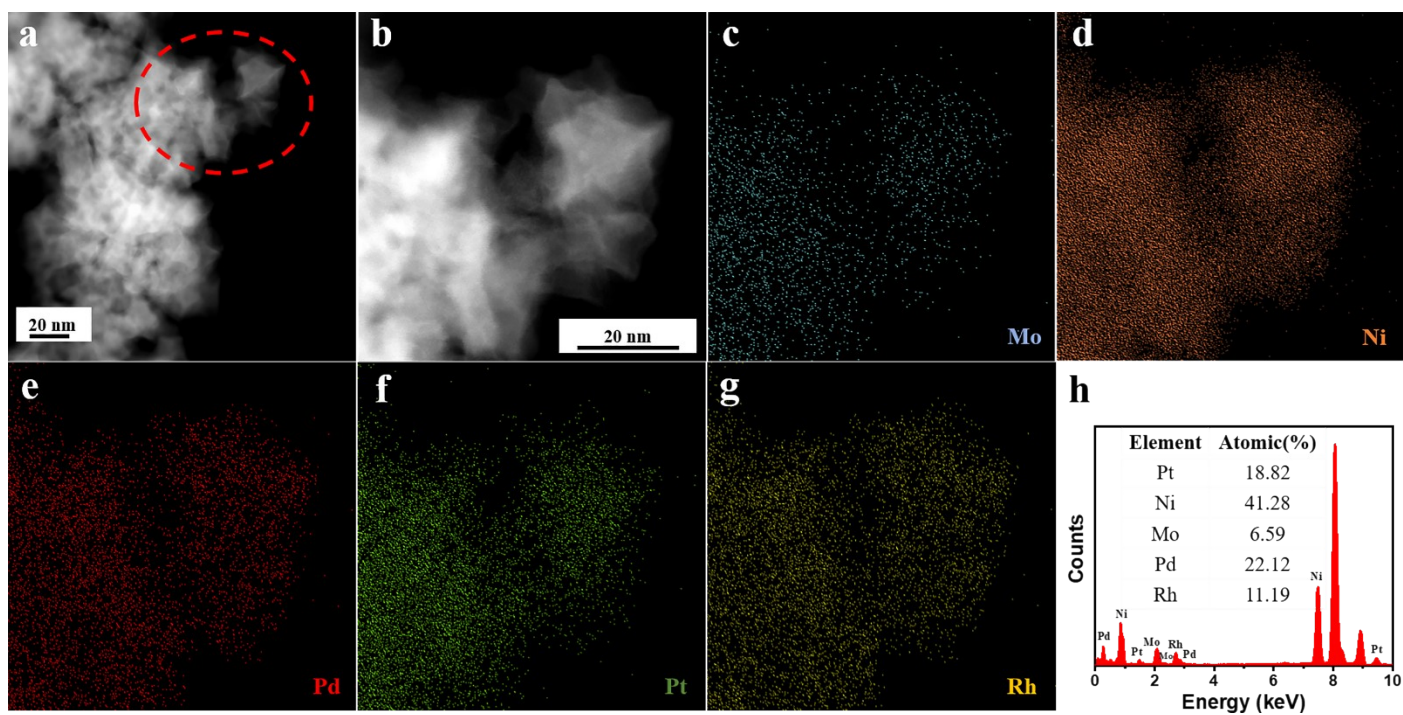
Figure S5. (a) (b) HADDF images, (c-g) elemental mapping, and (h) EDS spectrum and the corresponding atomic ratio of $Pt_{18}Mo_6Pd_{24}Rh_{12}Ni_{40}$ NCs.

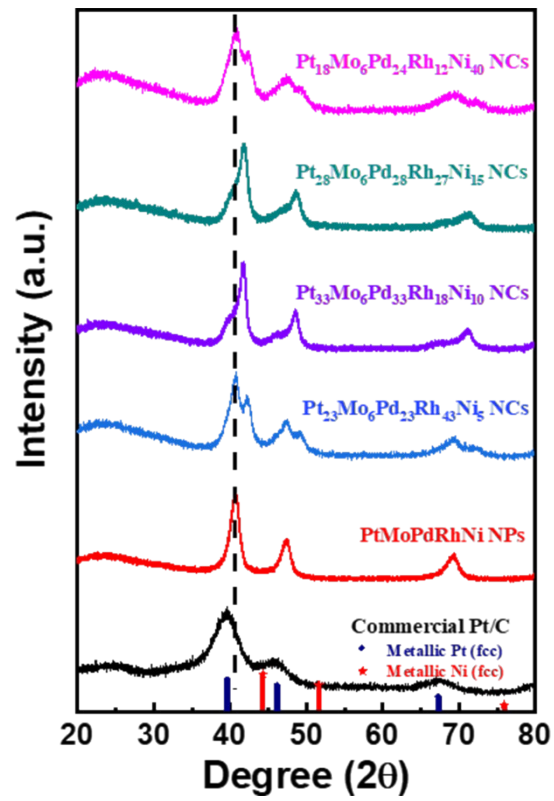| Element	Atomic(%)
Pt	18.82
Ni	41.28
Mo	6.59
Pd	22.12
Rh	11.19

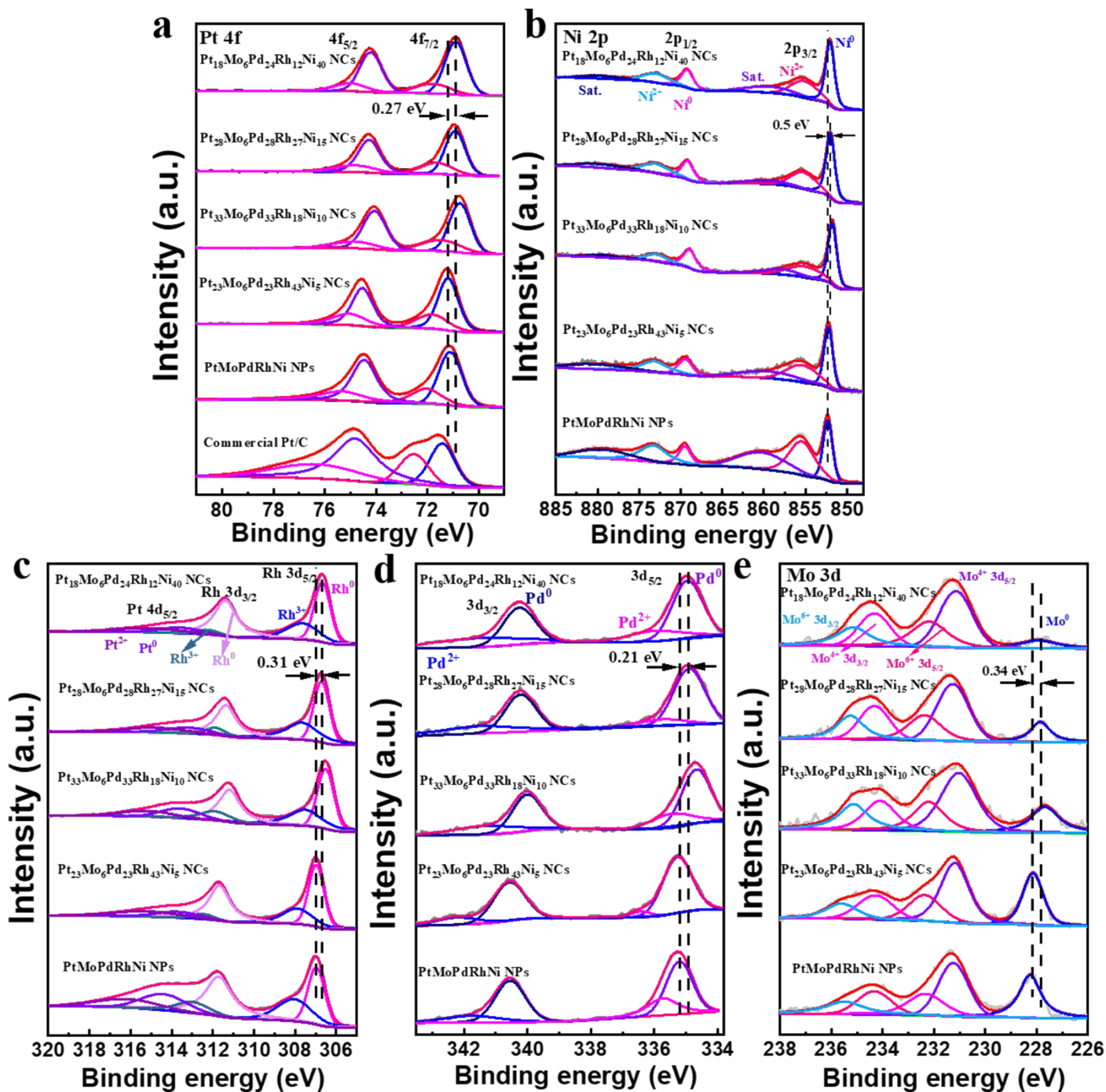**Figure S6.** XRD patterns of commercial Pt/C, PtMoPdRhNi NPs and PtMoPdRhNi NCs.

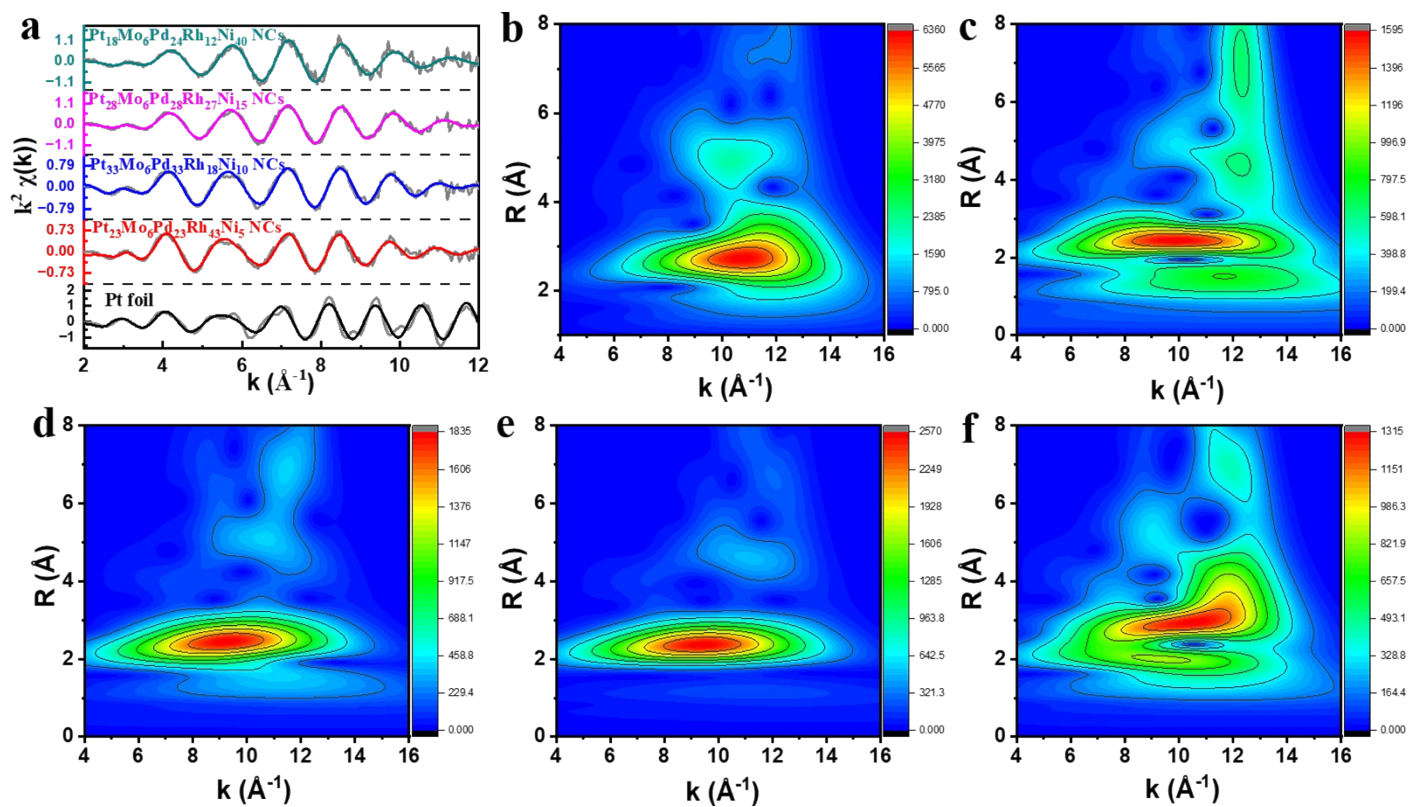**Figure S7.** XPS spectra of (a) Pt 4f, (b) Ni 2p, (c) Rh 3d, (d) Pd 3d, (e) Mo 3d of commercial Pt/C, PtMoPdRhNi NPs and PtMoPdRhNi NCs.

Figure S8. (a) k^2-weighted EXAFS in k space Pt L_3-edge in PtMoPdRhNi NCs, (b-f) Wavelet transformed XAS signal of Pt foil, $Pt_{23}Mo_6Pd_{23}Rh_{43}Ni_5$, $Pt_{33}Mo_6Pd_{33}Rh_{18}Ni_{10}$, $Pt_{28}Mo_6Pd_{28}Rh_{27}Ni_{15}$, $Pt_{18}Mo_6Pd_{24}Rh_{12}Ni_{40}$, respectively.

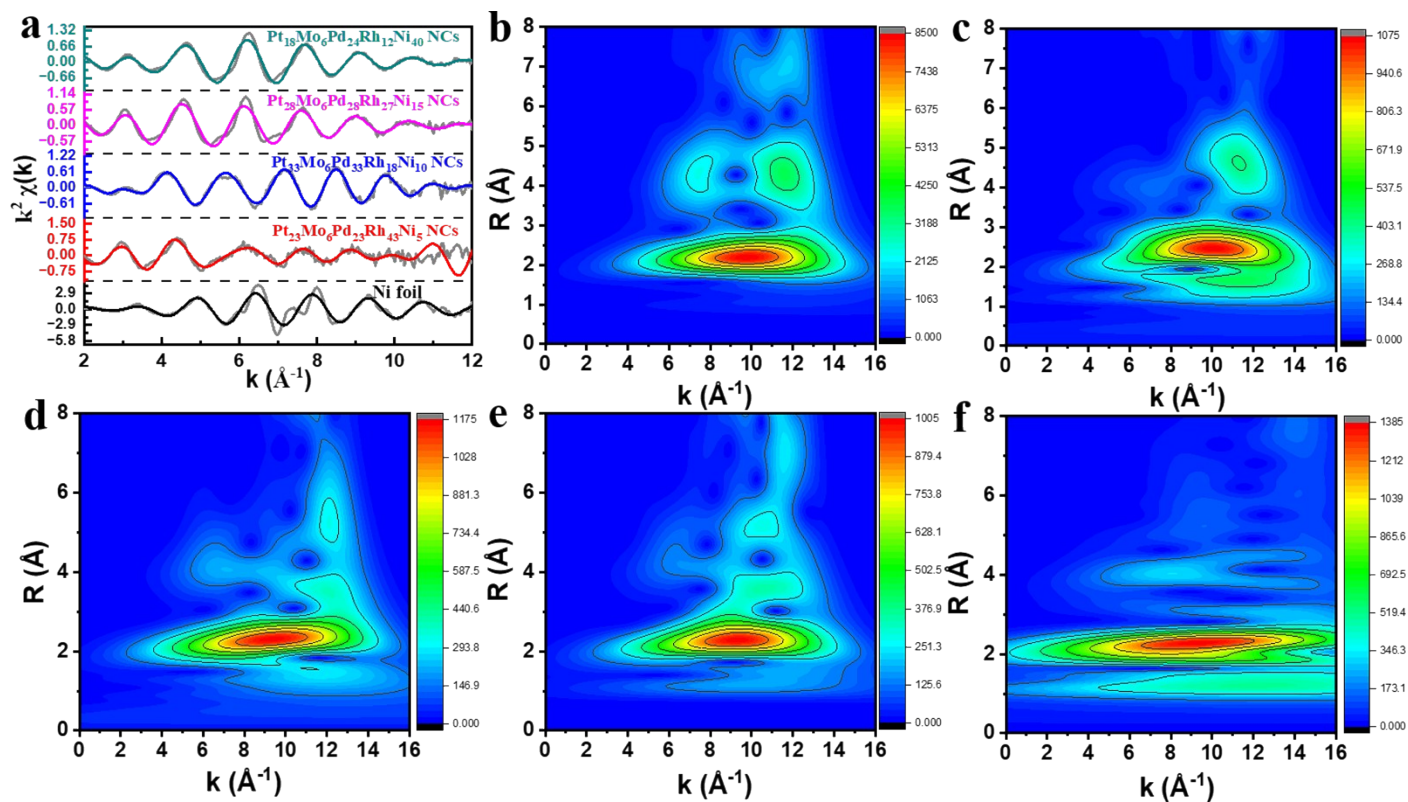**Figure S9.** (a) k^2-weighted EXAFS in k space of Ni K-edge in PtMoPdRhNi NCs, (b-f) Wavelet transformed XAS signal of Ni foil, $Pt_{23}Mo_6Pd_{23}Rh_{43}Ni_5$, $Pt_{33}Mo_6Pd_{33}Rh_{18}Ni_{10}$, $Pt_{28}Mo_6Pd_{28}Rh_{27}Ni_{15}$, $Pt_{18}Mo_6Pd_{24}Rh_{12}Ni_{40}$, respectively.
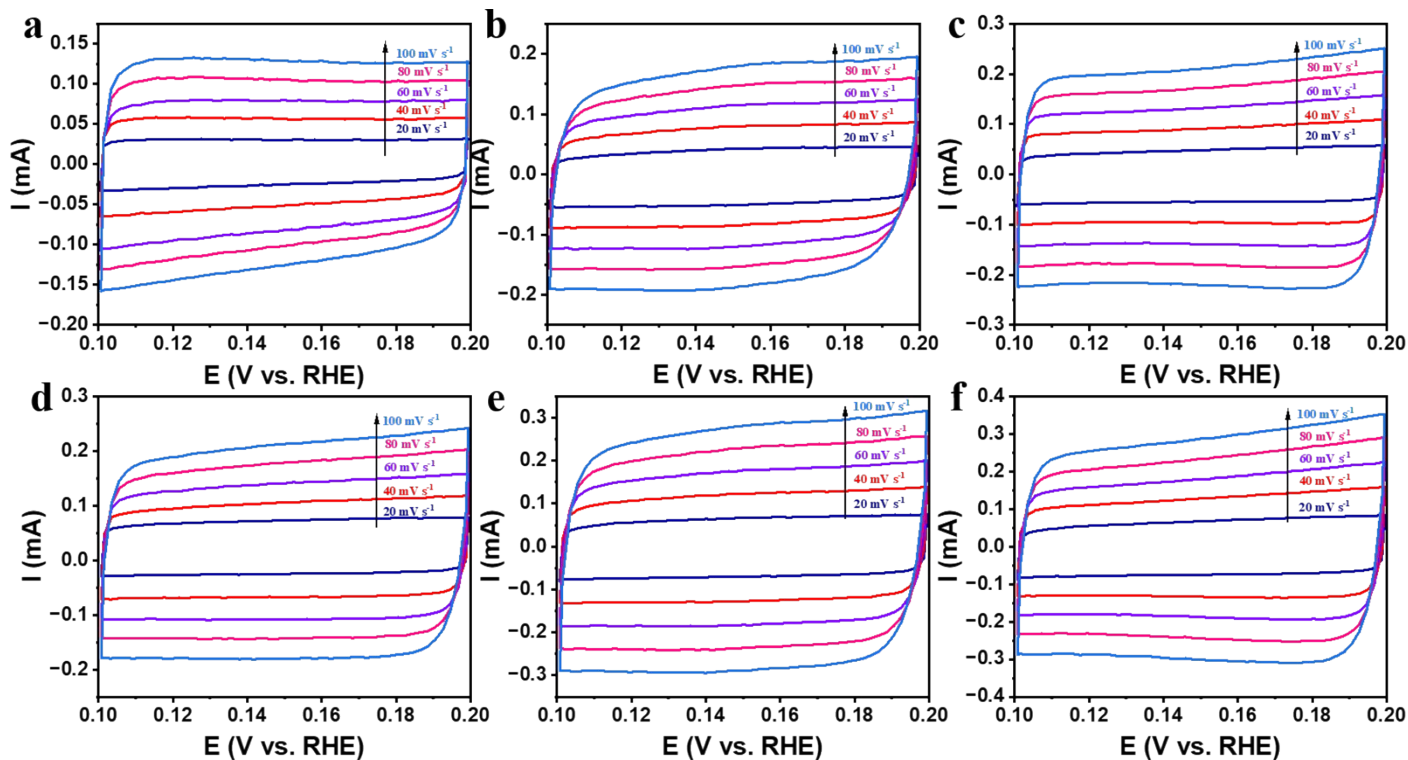
Figure S10. Typical CVs of the samples with scanning rates ranging from 20 to 100 mV s^{-1} of (a) commercia Pt/C, (b) PtMoPdRhNi NPs, (c) Pt$_{23}$Mo$_6$Pd$_{23}$Rh$_{43}$Ni$_5$ NCs, (d) Pt$_{33}$Mo$_6$Pd$_{33}$Rh$_{18}$Ni$_{10}$ NCs, (e) Pt$_{28}$Mo$_6$Pd$_{28}$Rh$_{27}$Ni$_{15}$ NCs, (f) Pt$_{18}$Mo$_6$Pd$_{24}$Rh$_{12}$Ni$_{40}$ NCs, respectively. The scanning potential range is from 0.10 V to 0.20 V in 1.0 M KOH solution.
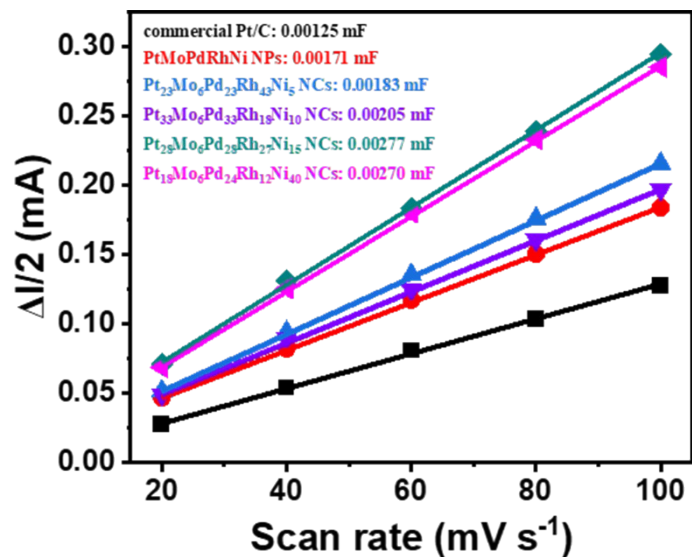
Figure S11. The estimation of C_{dl} by plotting the capacitive current density against the scan rate to fit a linear regression of PtMoPdRhNi NCs, PtMoPdRhNi NPs and commercial Pt/C.
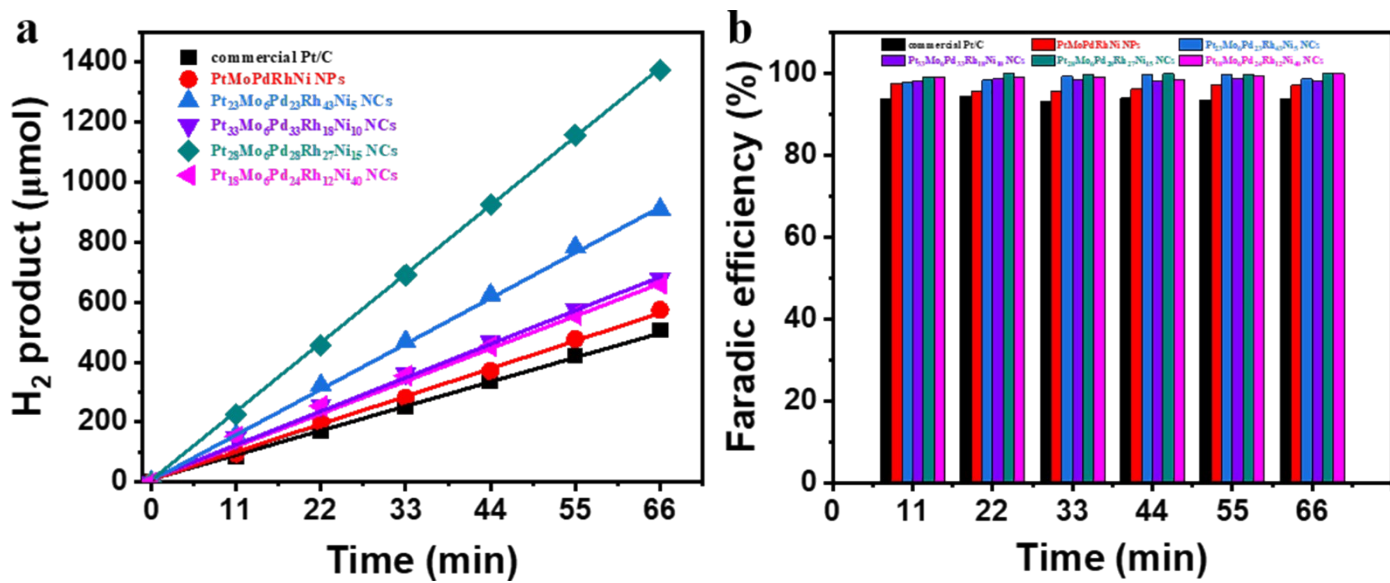
Figure S12. (a) H_2 product and (b) faradaic efficiency of commercial Pt/C, PtMoPdRhNi NPs and PtMoPdRhNi NCs at the overpotential of 100 mV.
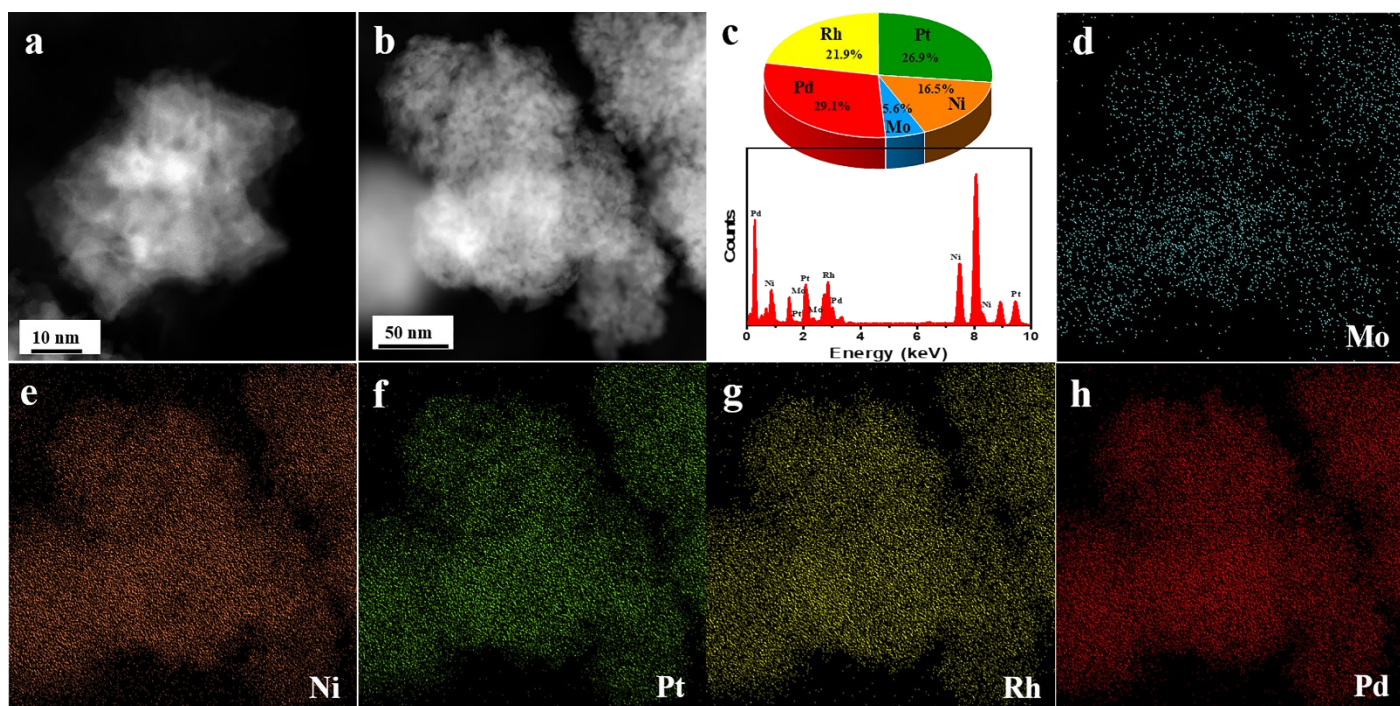
Figure S13. (a) (b) TEM images of $Pt_{28}Mo_6Pd_{28}Rh_{27}Ni_{15}$ NCs after 5,000 cycles for ADTs, (c) EDS spectrum and the corresponding atomic ratio, (d-h) EDS element mapping of (b).
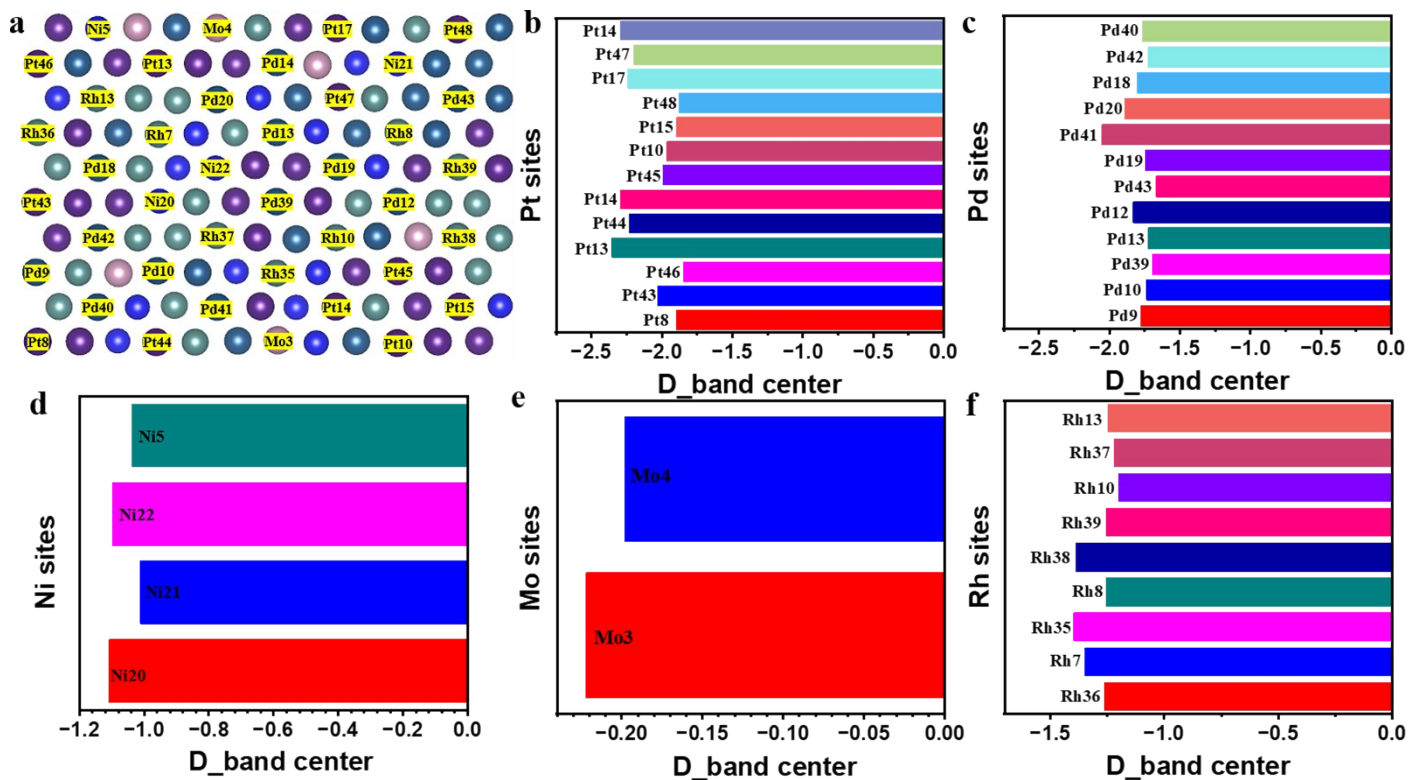
Figure S14. (a) the top view of calculation model with labels, (b) Pt sites, (c) Pd sites, (d) Rh sites, (e) Mo sites and (f) Rh sites with d band center of the surface constitute metals in $Pt_{30}Mo_5Pd_{25}Rh_{25}Ni_{15}$ (1 1 1).
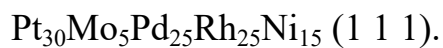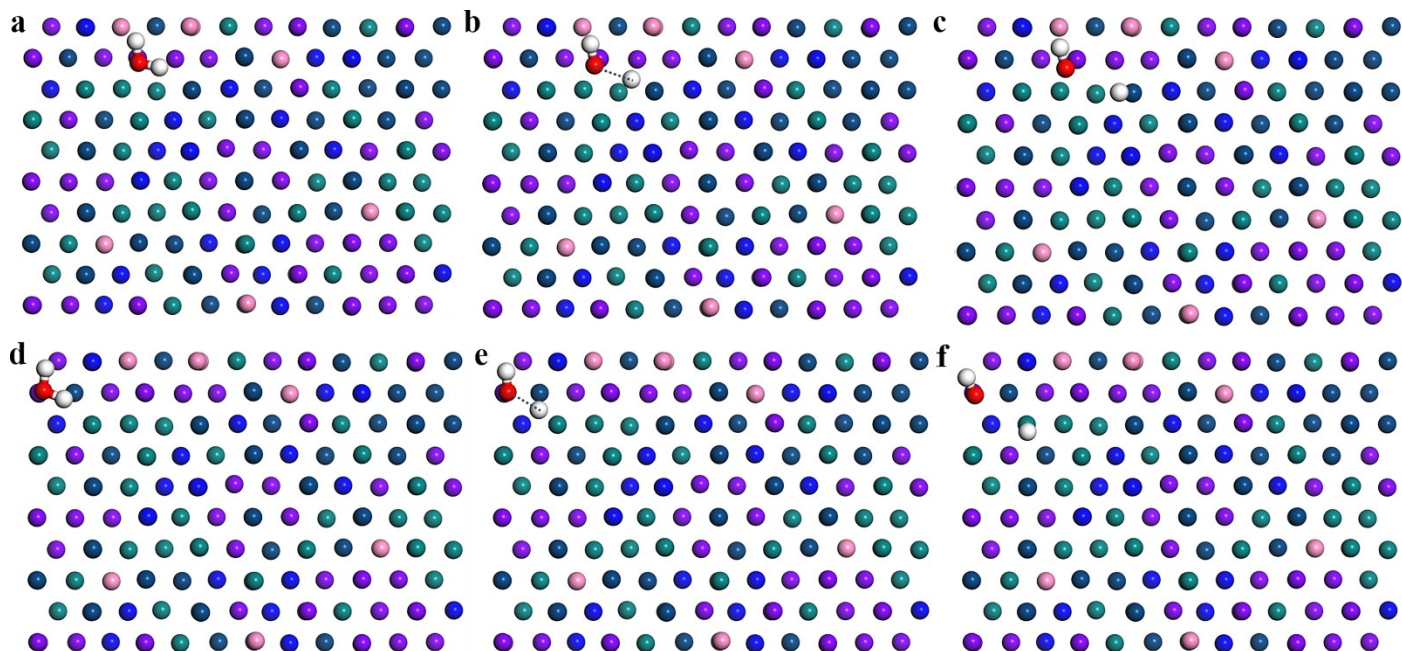
Figure S15. Binding configurations at (a-c) Pt13 and (d-f) Pt46.
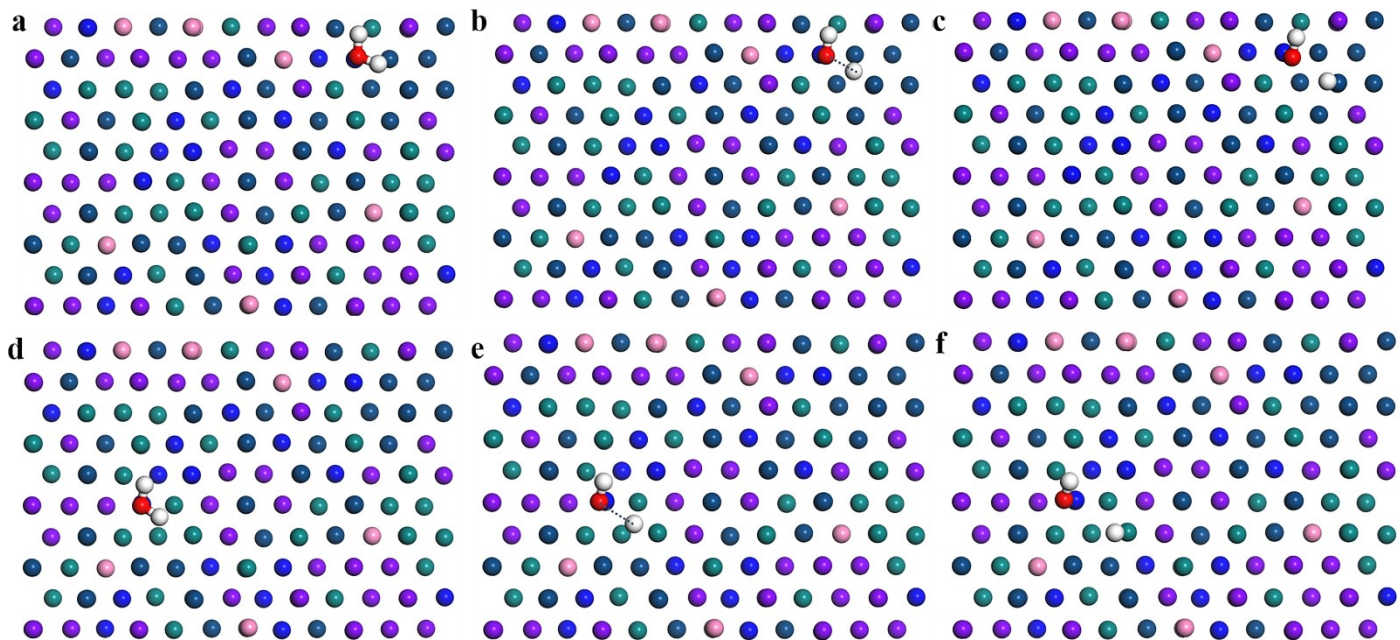
Figure S16. Binding configurations at (a-c) Ni21 and (d-f) Ni20.
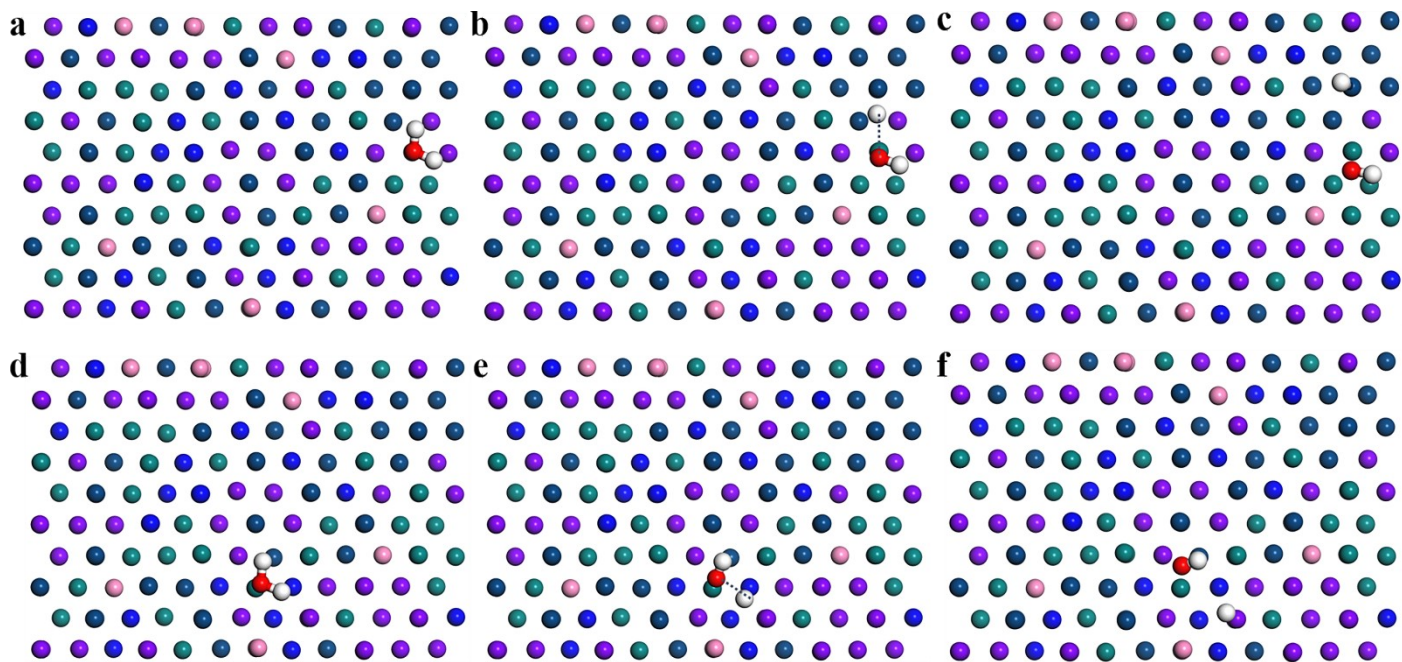
Figure S17. Binding configurations at (a-c) Rh39 and (d-f) Rh35.
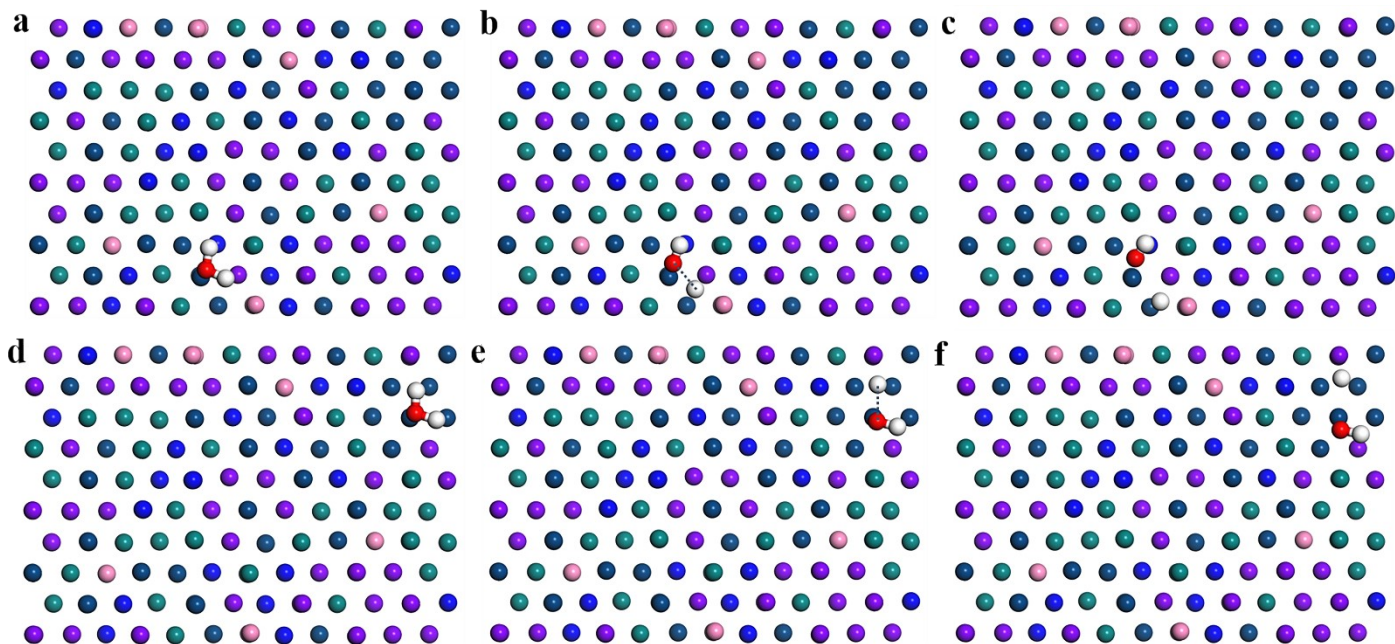
Figure S18. Binding configurations at (a-c) Pd41 and (d-f) Pd43.
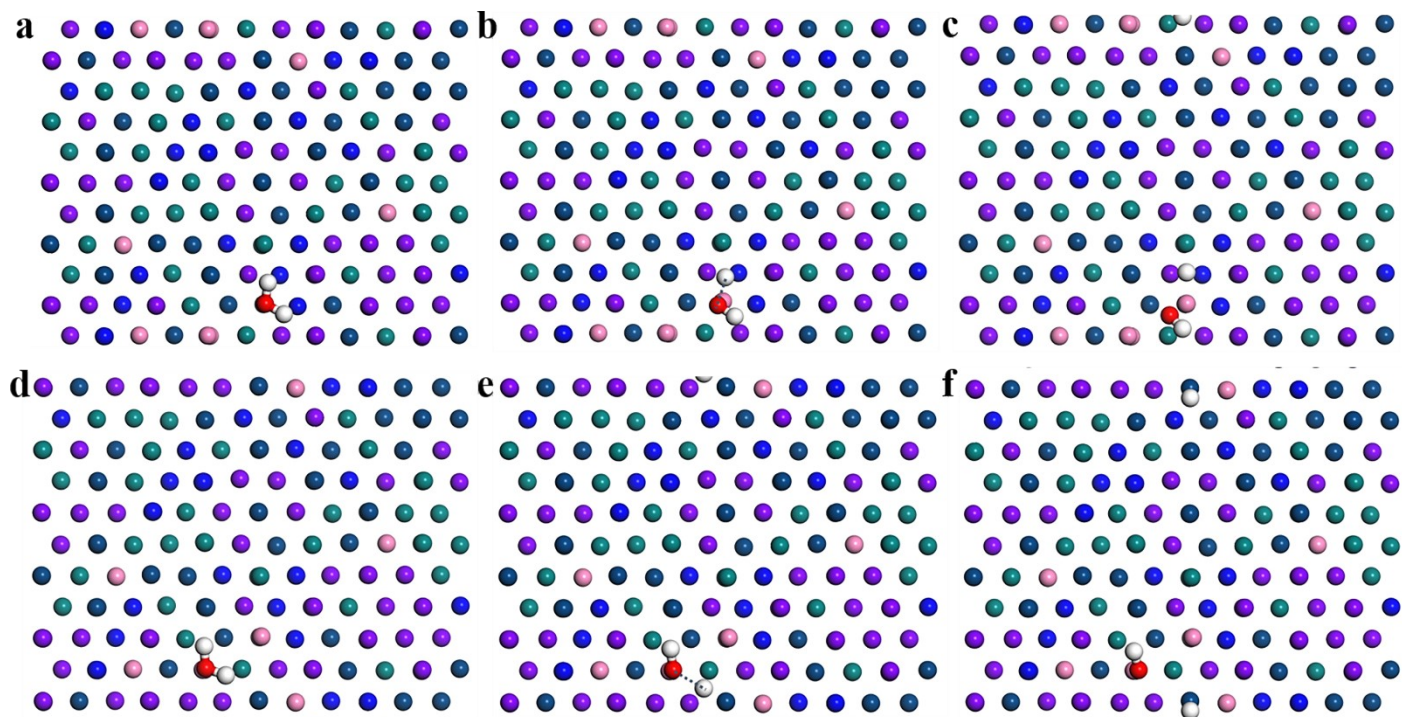
Figure S19. Binding configurations at (a-c) Mo3 and (d-f) Mo4.

Table S1. The ICP analysis of the PtMoPdRhNi NCs. The units are atomic percentages (atom%).

sample	Pt	Ni	Mo	Pd	Rh
$Pt_{23}Mo_6Pd_{23}Rh_{43}Ni_5$ NCs	23.1	5.3	6.2	23.2	42.2
$Pt_{33}Mo_6Pd_{33}Rh_{18}Ni_{10}$ NCs	33.2	10.4	6.1	33.2	17.1
$Pt_{28}Mo_6Pd_{28}Rh_{27}Ni_{15}$ NCs	28.3	15.3	6.1	27.8	22.5
$Pt_{18}Mo_6Pd_{24}Rh_{12}Ni_{40}$ NCs	18.2	40.2	6.3	23.7	11.6

Table S2. The fitted lattice parameters (interplanar spacing (d) and lattice constant) of PtMoPdRhNi NCs and PtMoPdRhNi NPs.

Catalysts	d (1 1 1) (Å)	d (2 0 0) (Å)	d (2 2 0) (Å)	Lattice constant (a=b=c, Å)
$Pt_{23}Mo_6Pd_{23}Rh_{43}Ni_5$ NCs	2.22	1.92	1.35	3.83
$Pt_{33}Mo_6Pd_{33}Rh_{18}Ni_{10}$ NCs	2.16	1.87	1.32	3.74
$Pt_{28}Mo_6Pd_{28}Rh_{27}Ni_{15}$ NCs	2.16	1.87	1.32	3.74
$Pt_{18}Mo_6Pd_{24}Rh_{12}Ni_{40}$ NCs	2.20	1.91	1.35	3.82
PtMoPdRhNi NPs	2.21	1.92	1.36	3.83

Table S3. Structural parameters of CN, bond distance (R), Debye factor (σ^2) and R factor from EXAFS fitting of Pt foil, PtMoPdRhNi NCs. The data is k^2-weighted and not phase-corrected, and the fitting range of PtMoPdRhNi NCs is $1.85 < k < 10.45$ Å^{-1}, $1.2 < R < 3.8$ Å.

Sample	Scatter path	CN	R/Å	σ^2/Å^2	R factor
Pt foil	Pt-Pt	12	2.76	0.003	0.9%
$Pt_{23}Mo_6Pd_{23}Rh_{43}Ni_5$ NCs	Pt-Pd	4.98 ± 1.37	2.67	0.0085	1.8%
	Pt-Ni	3.82 ± 0.97	2.69	0.0085	
	Pt-Pt	6.88 ± 2.31	2.70	0.0085	
$Pt_{33}Mo_6Pd_{33}Rh_{18}Ni_{10}$ NCs	Pt-Pd	1.71 ± 0.32	2.72	0.0006	0.9%
	Pt-Ni	7.96 ± 1.32	2.63	0.0006	
	Pt-Pt	2.84 ± 0.48	2.71	0.0006	
$Pt_{28}Mo_6Pd_{28}Rh_{27}Ni_{15}$ NCs	Pt-Pd	2.93 ± 0.86	2.68	0.0054	0.2%
	Pt-Ni	5.35 ± 0.73	2.62	0.0054	
	Pt-Pt	3.37 ± 1.17	2.68	0.0054	
$Pt_{18}Mo_6Pd_{24}Rh_{12}Ni_{40}$ NCs	Pt-Pd	2.69 ± 1.05	2.65	0.0085	1.0%
	Pt-Ni	6.65 ± 1.77	2.60	0.0085	
	Pt-Pt	4.04 ± 1.45	2.72	0.0085	

Table S4. Structural parameters of CN, bond distance (R), Debye factor (σ^2) and R factor from EXAFS fitting of Ni foil, PtMoPdRhNi NCs. The data is k^2-weighted and not phase-corrected, and the fitting range of PtMoPdRhNi NCs is 2.09 < k < 10.53 Å^{-1}, 1.0 < R < 3.6 Å.

Sample	Scatter path	CN	R/Å	σ^2/Å^2	R factor
Ni foil	Ni-Ni	12	2.48	0.0058	0.4%
Pt$_{23}$Mo$_6$Pd$_{23}$Rh$_{43}$Ni$_5$ NCs	Ni-Pt	2.59 ± 0.78	2.69	0.0006	2.3%
	Ni-Rh	1.92 ± 0.28	2.58	0.0006	
	Ni-Ni/Mo	0.75 ± 0.18	2.52/2.43	0.0006	
	Ni-O	0.74 ± 0.27	1.91	0.0006	
Pt$_{33}$Mo$_6$Pd$_{33}$Rh$_{18}$Ni$_{10}$ NCs	Ni-Pt	2.61 ± 1.29	2.63	0.0125	1.2%
	Ni-Rh	1.95 ± 0.75	2.63	0.0125	
	Ni-Ni	5.26 ± 1.20	2.59	0.0125	
	Ni-O	0.67 ± 0.27	1.96	0.0125	
Pt$_{28}$Mo$_6$Pd$_{28}$Rh$_{27}$Ni$_{15}$ NCs	Ni-Pt	1.27 ± 0.38	2.62	0.011	0.5%
	Ni-Rh	2.51 ± 0.83	2.62	0.011	
	Ni-Ni	6.35 ± 1.36	2.57	0.011	
	Ni-O	0.14 ± 0.05	1.97	0.011	
Pt$_{18}$Mo$_6$Pd$_{24}$Rh$_{12}$Ni$_{40}$ NCs	Ni-Pt	1.79 ± 0.74	2.60	0.011	1.3%
	Ni-Rh	1.98 ± 0.07	2.61	0.011	
	Ni-Ni	6.94 ± 1.32	2.56	0.011	
	Ni-O	1.21 ± 0.39	2.08	0.011	

Table S5. Comparison of PtMoPdRhNi NCs and reported Pt-based/ HEA catalysts for HER in 1 M KOH.

Catalysts	Noble metal loading ($\mu g\ cm^{-2}$)	Overpotential @-10mA cm^{-2} (mV)	Tafel slope (mV dec^{-1})
$Pt_{28}Mo_6Pd_{28}Rh_{27}Ni_{15}$ NCs	21.44	9.7	25.9
$Pt_{23}Mo_6Pd_{23}Rh_{43}Ni_5$ NCs	21.44	15.9	30.3
$Pt_{18}Mo_6Pd_{24}Rh_{12}Ni_{40}$ NCs	21.44	20.1	30.5
$Pt_{33}Mo_6Pd_{33}Rh_{18}Ni_{10}$ NCs	21.44	22.2	26.9
FeCoNiAlTi[12]	-	88.2	40.1
FeCoPdIrPt[13]	-	42	82
$Pt_{18}Ni_{26}Fe_{15}Co_{14}Cu_{27}$[14]	-	44	41
PdFeCoNiCu[15]	-	18	39
IrPdPtRhRu[16]	-	17	
Nanosponge-like PdPtCuNiP[17]	-	32	37.4
PtSn@PtCo Heterojunction[18]	-	25	24
PtNi$_5$-0.3[19]	-	26.8	19.2
Pt Clusters@MXene[20]	42.1	34	29.7
Dp-Pt[21]	10	25	52
PtSe$_2$/Pt Heterointerface[22]	-	42	53
CNs@CoPt[23]		19.1	54.3
Pt on NiRu-hydroxide[24]	-	38	39
NF-Na-Fe-Pt[25]	-	31	35.98
Pt-V$_2$CTx[26]	16	68.1	98.6
Pt/PtTex[27]	-	23	23
PtNi Ass[28]	-	27.5	27
PtNi@Ti$_3$C$_2$ MXenes[29]	-	36	59
Pt–Ni(N) NWs[30]	17	13	29
PtRu NCs/BP[31]	-	22	43
Pt–Ni NTAs[32]	56	23	38
PtSA-NiO/Ni[33]	14.8	26	27.07
Pt-NiNWs[34]	-	40	-
Pt NWs/SL-Ni(OH)$_2$[35]	-	70	-
FeCoNiCuPd thin-film[36]	15.3	29	47.2

Table S6. The electrochemical impedance spectra fitting results of PtMoPdRhNi NCs, PtMoPdRhNi NPs and commercial Pt/C. (Rs: solution resistance; Rct: charge transfer resistance)

Catalysts	Rs	Rct
$Pt_{23}Mo_6Pd_{23}Rh_{43}Ni_5$ NCs	4.5	5.1
$Pt_{33}Mo_6Pd_{33}Rh_{18}Ni_{10}$ NCs	4.9	8.5
$Pt_{28}Mo_6Pd_{28}Rh_{27}Ni_{15}$ NCs	4.7	3.1
$Pt_{18}Mo_6Pd_{24}Rh_{12}Ni_{40}$ NCs	4.7	4.8
PtMoPdRhNi NPs	4.3	11.9
Commercial Pt/C	6.3	36.9

Table S7. A series of DFT results identifying the stable adsorption sites of H* on $Pt_{30}Mo_5Pd_{25}Rh_{25}Ni_{15}$ (1 1 1) surfaces and its corresponding ΔG_{H*} (eV).

Initial position	Optimized position	ΔG_{H*}
Pt top	Pt top	-0.01
Pt top	Pt-Rh-Mo	-0.14
Pd top	Ni-Rh-Pd	-0.14
Pd top	Rh-Pd-Rh	-0.17
Pt top	Pt top	-0.12
Pt top	Pt top	-0.06
Pt top	Pd-Pd-Pt	-0.01
Pt top	Mo-Pd-Pt	-0.15
Pt top	Pt-Ni-Rh	-0.04
Pt top	Pt top	-0.17
Ni top	Ni-Rh-Ni	-0.18
Rh top	Rh top	-0.03
Rh top	Pd-Rh-Rh	-0.14
Rh top	Rh top	-0.07
Rh top	Pd-Rh-Pd	-0.09
Pd top	Pd-Pd-Ni	-0.25
Pd top	Rh top	-0.07
Pd top	Pd-Pd-Pd	0.06
Pd top	Rh-Pd-Pd	-0.07
Pd top	Pt-Pd-Pd	-0.25
Pd top	Pd-Pd bridge	-0.06
Pd top	Pd-Mo-Rh	-0.09
Mo top	Ni-Rh-Pd	-0.12
Mo top	Mo-Mo-Pd	-0.28
Pt top	Pt top	-0.10
Pt top	Pt top	-0.16
Pt top	Pt top	-0.15
Pt top	Pt top	-0.16
Pd top	Pd-Pd-Ni	-0.03
Ni top	Ni top	0.27
Ni top	Pt-Pd-Ni	-0.01
Ni top	Pd-Rh-Ni	-0.25
Rh top	Pd-Rh-Pd	-0.12
Rh top	Pd-Rh-Mo	-0.09
Rh top	Rh top	-0.08
Rh top	Rh top	-0.12
Pd top	Pd-Rh bridge	0.18
Pd top	Pd-Pd-Pd	-0.24
Pd top	Pd-Pd bridge	0.19
Rh top	Pd-Rh-Rh	-0.32

1. B. Ravel and M. Newville, *J. Synchrotron Radiat*, 2005, **12**, 537-541.
2. Y.-Y. Ma, C.-X. Wu, X.-J. Feng, H.-Q. Tan, L.-K. Yan, Y. Liu, Z.-H. Kang, E.-B. Wang and Y.-G. Li, *Energy Environ. Sci.*, 2017, **10**, 788-798.
3. D. H. Kweon, M. S. Okyay, S. J. Kim, J. P. Jeon, H. J. Noh, N. Park, J. Mahmood and J. B. Baek, *Nat. Commun.*, 2020, **11**, 1278.
4. G. Kresse and J. Hafner, *Phys. Rev. B Condens Matter.*, 1994, **49**, 14251-14269.
5. G. Kresse and J. Hafner, *Phys. Rev. B Condens Matter.*, 1993, **47**, 558-561.
6. P. E. Blochl, *Phys. Rev. B Condens. Matter.*, 1994, **50**, 17953-17979.
7. J. P. Perdew, K. Burke and M. Ernzerhof, *Phys. Rev. Lett.*, 1996, **77**, 3865-3868.
8. A. Zunger, S. Wei, L. G. Ferreira and J. E. Bernard, *Phys Rev Lett*, 1990, **65**, 353-356.
9. A. v. d. Walle, P. Tiwary, M. d. Jong, D. L. Olmsted, M. Asta, A. Dick, D. Shin, Y. Wang, L.-Q. Chen and Z.-K. Liu, *CALPHAD: Computer Coupling of Phase Diagrams and Thermochemistry*, 2013, **42**, 13-18.
10. T. A. A. Batchelor, J. K. Pedersen, S. H. Winther, I. E. Castelli, K. W. Jacobsen and J. Rossmeisl, *Joule*, 2019, **3**, 834-845.
11. R. B. Wexler, J. M. P. Martirez and A. M. Rappe, *J. Am. Chem. Soc.*, 2018, 140, 4678-4683.
12. Z. Jia, T. Yang, L. Sun, Y. Zhao, W. Li, J. Luan, F. Lyu, L. C. Zhang, J. J. Kruzic, J. J. Kai, J. C. Huang, J. Lu and C. T. Liu, *Adv. Mater.*, 2020, **32**, e2000385.
13. S. Gao, S. Hao, Z. Huang, Y. Yuan, S. Han, L. Lei, X. Zhang, R. Shahbazian-Yassar and J. Lu, *Nat. Commun.*, 2020, **11**, 2016.
14. H. Li, Y. Han, H. Zhao, W. Qi, D. Zhang, Y. Yu, W. Cai, S. Li, J. Lai, B. Huang and L. Wang, *Nat. Commun.*, 2020, **11**, 5437.
15. D. Zhang, Y. Shi, H. Zhao, W. Qi, X. Chen, T. Zhan, S. Li, B. Yang, M. Sun, J. Lai, B. Huang and L. Wang, *J. Mater. Chem. A*, 2021, **9**, 889-893.
16. D. Wu, K. Kusada, T. Yamamoto, T. Toriyama, S. Matsumura, I. Gueye, O. Seo, J. Kim, S. Hiroi, O. Sakata, S. Kawaguchi, Y. Kubota and H. Kitagawa, *Chem. Sci.*, 2020, **11**, 12731-12736.
17. Z. Jia, K. Nomoto, Q. Wang, C. Kong, L. Sun, L. C. Zhang, S. X. Liang, J. Lu and J. J. Kruzic, *Adv. Funct. Mater.*, 2021, **31**, 2101586.
18. J. Chen, G. Qian, H. Zhang, S. Feng, Y. Mo, L. Luo and S. Yin, *Adv. Funct. Mater.*, 2021, **32**, 2107597.
19. C. Zhang, X. Liang, R. Xu, C. Dai, B. Wu, G. Yu, B. Chen, X. Wang and N. Liu, *Adv. Funct. Mater.*, 2021, **31,** 2008298.
20. Y. Wu, W. Wei, R. Yu, L. Xia, X. Hong, J. Zhu, J. Li, L. Lv, W. Chen, Y. Zhao, L. Zhou and L. Mai, *Adv. Funct. Mater.*, 2022, **32**, 2110910.
21. S. Liu, Y. Shen, Y. Zhang, B. Cui, S. Xi, J. Zhang, L. Xu, S. Zhu, Y. Chen, Y. Deng and W. Hu, *Adv. Mater.*, 2022, **34**, e2106973.
22. Z. Wang, B. Xiao, Z. Lin, Y. Xu, Y. Lin, F. Meng, Q. Zhang, L. Gu, B. Fang, S. Guo and W. Zhong, *Angew. Chem. Int. Ed. Engl.*, 2021, **60**, 23388-23393.
23. S. Li, W. Xie, Y. Song, Y. Li, Y. Song, J. Li and M. Shao, *Chem. Eng. J.*, 2022, **437**, 135473.
24. D. Li, X. Chen, Y. Lv, G. Zhang, Y. Huang, W. Liu, Y. Li, R. Chen, C. Nuckolls and H. Ni, *Appl. Catal. B.,* 2020, **269**, 118824.
25. Y. Zhao, Y. Gao, Z. Chen, Z. Li, T. Ma, Z. Wu and L. Wang, *Appl. Catal. B.*, 2021, **297**, 120395.
26. S. Park, Y.-L. Lee, Y. Yoon, S. Y. Park, S. Yim, W. Song, S. Myung, K.-S. Lee, H. Chang, S. S. Lee and K.-S. An, *Appl. Catal. B.*, 2022, **304**, 120989.
27. J. Chen, M. Qin, S. Ma, R. Fan, X. Zheng, S. Mao, C. Chen and Y. Wang, *Appl. Catal. B.*, 2021, **299**, 120640.
28. Z. Zhang, G. Liu, X. Cui, B. Chen, Y. Zhu, Y. Gong, F. Saleem, S. Xi, Y. Du, A. Borgna, Z. Lai, Q. Zhang, B. Li, Y. Zong, Y. Han, L. Gu and H. Zhang, *Adv. Mater.*, 2018, **30**, e1801741.
29. Y. Yan, R. Zhang, Y. Yu, Z. Sun, R. Che, B. Wei, A. P. LaGrow, Z. Wang and W. Zhou, *Appl. Catal.*

B., 2021, **291**, 120100.

30. Y. Xie, J. Cai, Y. Wu, Y. Zang, X. Zheng, J. Ye, P. Cui, S. Niu, Y. Liu, J. Zhu, X. Liu, G. Wang and Y. Qian, *Adv. Mater.*, 2019, **31**, e1807780.

31. Y. Li, W. Pei, J. He, K. Liu, W. Qi, X. Gao, S. Zhou, H. Xie, K. Yin, Y. Gao, J. He, J. Zhao, J. Hu, T.-S. Chan, Z. Li, G. Zhang and M. Liu, *ACS Catal.*, 2019, **9**, 10870-10875.

32. A. Nairan, C. Liang, S.-W. Chiang, Y. Wu, P. Zou, U. Khan, W. Liu, F. Kang, S. Guo, J. Wu and C. Yang, *Energy Environ.*, 2021, **14**, 1594-1601.

33. K. L. Zhou, Z. Wang, C. B. Han, X. Ke, C. Wang, Y. Jin, Q. Zhang, J. Liu, H. Wang and H. Yan, *Nat. Commun.*, 2021, **12**, 3783.

34. P. Wang, K. Jiang, G. Wang, J. Yao and X. Huang, *Angew Chem Int Ed Engl*, 2016, **55**, 12859-12863.

35. H. Yin, S. Zhao, K. Zhao, A. Muqsit, H. Tang, L. Chang, H. Zhao, Y. Gao and Z. Tang, *Nat. Commun.*, 2015, **6**, 6430.

36. S. Wang, B. Xu, W. Huo, H. Feng, X. Zhou, F. Fang, Z. Xie, J. K. Shang and J. Jiang, *Appl. Catal. B.*, 2022, **313**, 121472.